Preparation and Electrochemical Performance of Nano-LiNi$_{0.05}$Mn$_{1.95}$O$_4$ Cathode Materials by a Low-Temperature Molten-Salt Combustion Method

Wangqiong Xu[1,2], Hongli Bai[1,2], Qiling Li[1,2], Tao Feng[1,2], Junming Guo[1,2,],*
Lili Feng[1,2], Chang-wei Su[1,2], Wei Bai[1,2], Xiaofang Liu[1,2]

[1] Key Laboratory of Resource Clean Conversion in Ethnic Regions，Education Department of Yunnan, Yunnan Minzu University, Kunming 650500, PR China
[2] Joint Research Centre for International Cross-border Ethnic Regions Biomass Clean Utilization in Yunnan, Yunnan Minzu University, Kunming 650500, PR China
[*]E-mail: guojunming@tsinghua.org.cn

Nano-LiNi$_{0.05}$Mn$_{1.95}$O$_4$ cathode materials with nano-sized particles were successfully synthesized by a low temperature molten-salt combustion method at 400 ℃ for 1 h and then two-stage calcination at 600 ℃ for 3 h. The crystal structures and morphologies of nano-LiNi$_{0.05}$Mn$_{1.95}$O$_4$ were characterized by X-ray diffraction (XRD), X-ray photoelectron spectroscopy (XPS), scanning electron microscopy (SEM) and transmission electron microscopy (TEM). All obtained samples with good crystallinity were identified as the cubic spinel structure of LiMn$_2$O$_4$. The lattice parameters and the particle size of samples decreased as the Ni doped. The effects of Ni^{2+} ion doping on the electrochemical properties of nano-LiNi$_{0.05}$Mn$_{1.95}$O$_4$ were investigated by a galvanostatic charge-discharge test, cyclic voltammetry (CV) and electrochemical impedance spectroscopy (EIS). The results showed that the nano-LiNi$_{0.05}$Mn$_{1.95}$O$_4$ sample exhibited the initial discharge capacity of 112.4 mAh g^{-1} with capacity retention of 80.7% after 1000 cycles at 1.0 C (1 C = 148.0 mAh g^{-1}). In addition, the nano-LiNi$_{0.05}$Mn$_{1.95}$O$_4$ sample exhibited good rate capabilities at different current densities from 0.5 C to 5.0 C. These improvements are attributed to the synergistic effects of the nano-structure and nickel doping of the LiNi$_{0.05}$Mn$_{1.95}$O$_4$ sample.

1. INTRODUCTION

Rechargeable Li-ion batteries (LIBs) are the most attractive energy-storage devices for powering electric vehicles (EVs) and hybrid electric vehicles (HEVs) [1-3]. The increasing demand for

reliable high energy density power sources has significantly increased the research and development of LIBs [4]. Currently, there are three primary structure types of cathode materials for LIBs: the layered-type $LiCoO_2$ and $LiNiO_2$, the olivine-type $LiFePO_4$ and the spinel-type $LiMn_2O_4$ [5-8]. Among these cathode materials, spinel $LiMn_2O_4$ is considered to be one of the most promising cathode materials for lithium ion batteries because it is cost effective, safe, environmentally friendly and easy to produce [9-11]. However, spinel $LiMn_2O_4$ suffers severe capacity fading during the charge-discharge cycling, which is most strongly related with the Jahn-Teller distortion, the dissolution of manganese and electrolyte decomposition [12-14]. To restrict the Jahn-Teller distortion effect, doping the manganese sites with other cations has been widely considered as an effective approach to improve the stability of MnO_6 octahedra and cyclability. According to the existing literatures [15-21], various divalent, trivalent and tetravalent-doped ions, such as Fe, Cu, Ga, Al, Ni, Ti, Si and so on, can contribute to the stability of the spinel structure and suppression of the Jahn-Teller distortion. Among these dopants, Ni has been expected to be a favorable dopant because the bond energy of the Ni-O (1029 kJ mol^{-1}) is strengther than that of the Mn-O bond (946 kJ mol^{-1}), which can lead to the lattice parameter decreased with an increase in the Ni-substitution and enhance the stability of octahedral sites in the spinel structure by inhibiting the Jahn-Teller distortion [22, 23]. Wei et al. [24] prepared spherical concentration-gradient material with an average composition of $LiMn_{1.87}Ni_{0.13}O_4$ using a co-precipitation route, and delivered a discharge capacity of 108.2 mAh g^{-1} between 3.0 and 4.4 V vs. Li/Li^+ with a retention of 90.2% over 200 cycles at a rate of 0.5 C at 55 °C. Kebede et al. [25] reported that spherically shaped Ni-substituted $LiNi_xMn_{2-x}O_4$ (x=0, 0.1 and 0.2) spinel cathode materials were synthesized by the solution-combustion technique. They demonstrated that first discharge capacity of Ni ion substituted samples $LiNi_xMn_{2-x}O_4$ (x=0.1, 0.2) were 116.4 and 110.5 mAh g^{-1} at 0.2 C, respectively, and the capacity retention reached 99% after 100 cycles. The nanosized $LiNi_{0.05}Mn_{1.95}O_4$ sample was synthesized by a sucrose-aided combustion method using Li(I), Mn(II), Ni(II) nitrate as raw materials and the raw materials were dissolved in the distilled water, and the fuel was then added to the solution. After slow evaporation at 120 °C a voluminous foamy mass was obtained. Then it spontaneously burned and transformed into a black sponge-like fluffy product. The as-prepared samples were additionally heated at 700 °C for 1 h. The galvanostatic charge-discharge result shows that the nanosized $LiNi_{0.05}Mn_{1.95}O_4$ sample exhibits a discharge capacity of 113.3 mAh g^{-1} with a retention of 95.1% over 100 cycles at 0.5 C charge and 1 C discharge rates [26].

On the other hand, the particle size, synthesis method and phase crystallinity have strongly influence on electrochemical properties of cathode material [27]. The nanostructured $LiMn_2O_4$ has been proven to be an effective strategy to improve its electrochemical performance, because lithium-ion-diffusion distances are dramatically reduced and the contact area is increased between the electrode and the electrolyte [28]. Ding et al. [29] studied that one-dimensional $LiAl_{0.05}Ni_{0.05}Mn_{1.95}O_4$ nanofibers are prepared by electrospinning method and obtained the discharge capacities of 133 and 110 mAh g^{-1} at 0.5 C and 10 C, and the capacity retention of 82.0% after 400 cycles at 0.5 C. Gao et al. [30] synthesized nanocrystalline $LiMn_2O_4$ by a cellulose-assisted combustion method and the discharge capacity were 114 mAh g^{-1} and 84 mAh g^{-1} at 0.2 C and 5 C.

In this study, the nano-$LiNi_{0.05}Mn_{1.95}O_4$ particles were successfully synthesized by a low temperature molten-salt combustion method. Lithium acetate, manganese acetate and nickel acetate

with low melting points of 59, 67 and 115 °C were used as raw materials and the raw materials self-mix upon heating. The crystal structure, morphology and electrochemical properties of the nano-$LiNi_{0.05}Mn_{1.95}O_4$ material were studied in detail. The electrochemical study revealed that the nano-$LiNi_{0.05}Mn_{1.95}O_4$ sample presented better electrochemical properties with excellent cycling retention and superior rate performance in comparison with the $LiMn_2O_4$ cathode.

2. EXPERIMENTAL

2.1. Preparation of samples

The nano-$LiNi_{0.05}Mn_{1.95}O_4$ sample was synthesized by a low temperature molten-salt combustion method. $CH_3COOLi \cdot 2H_2O$ (AR, Aladdin) and $Mn(CH_3COO)_2 \cdot 4H_2O$ (AR, Aladdin) with low melting points of 59 and 67 °C were used as lithium and manganese resources, $Ni(CH_3COO)_2 \cdot 4H_2O$ (AR, Sinopharm) with low melting points of 115 °C acted as dopant. The preparation of nano-$LiNi_{0.05}Mn_{1.95}O_4$ was as follows: 7.9212 g manganese acetate, 1.6909 g lithium acetate and 0.2062 g nickel acetate were successively put into a 300 mL ceramic crucible. Here the stoichiometric molar ratio was 1:1.95:0.05 (Li : Mn :Ni). The reactants were consecutively heated up to their eutectic temperature (70 ℃) in a muffle furnace at the constant temperature of 400 ℃, which was then heated to boil in order to make uniformly mixing of reactants in a ceramic crucible [31, 32], and this method of mixtures was also called furnace method [33, 34]. The reactants were continuously heated to burn the acetate ions in the acetate to obtain the one-stage materials (i.e. combustion products) at 400 ℃. The times of heating and combustion reaction were 1 h. The combustion products was cooled down to room temperature and grounded and then two-stage calcination at 600 ℃ for 3 h to obtain the black nano-$LiNi_{0.05}Mn_{1.95}O_4$ sample.

2.2. Characterization

The crystalline structure of samples was characterized by X-ray diffraction (XRD; D/max-TTRIII, Rigaku, Japan) with Cu Kα radiation in the 2θ angular range of 10-70° with a step size of 0.02° and scan speed of 4° min^{-1} at an operating current of 30 mA and voltage of 40 kV. Lattice parameters were obtained using Jade 5.0 software. The particle morphology of the materials was determined by a scanning electron microscopy (SEM, Nova NanoSEM 450, America FEI). Particle sizes were measured by a transmission electron microscope (TEM, JEM-2100), and the value of *d*-spacing was measured by Digital Micrograph software.

2.3. Electrochemical measurements

The nano-$LiNi_{0.05}Mn_{1.95}O_4$ electrodes were prepared by mixing the nano-$LiNi_{0.05}Mn_{1.95}O_4$ powders, carbon black and polyvinylidene fluoride (PVDF) with a mass ratio of 8:1:1. Then, N-methyl-2-pyrrolidon (NMP) was added to the mixture to form a homogeneous slurry. The slurry was

pasted onto an Al foil current collector and dried at 120 °C under a vacuum oven overnight. The cathodes were punched into disks with a diameter of 16 mm. For the electrochemical measurements, CR2025 coin-type cells were assembled in an argon-filled glove box using an nano-$LiNi_{0.05}Mn_{1.95}O_4$ cathode, Li foil anode, polypropylene microporous film (Celgard 2320) separator, and then the 1.0 M $LiPF_6$ electrolyte was dissolved in ethylene carbonate and dimethyl carbonate (1:1 in volume). Galvanostatic charge-discharge tests of the cells were performed using a Land electric test system (Wuhan Land Electronics Co., Ltd., China) between 3.0 and 4.5 V (vs. Li/Li$^+$) at room temperature. Cyclic voltammetry (CV) was conducted on a CHI604E electrochemical workstation (Shanghai Chenhua Instruments Co., Ltd., China) in the voltage range of 3.6-4.5 V. EIS spectra of cells were measured using the same electrochemical workstation in a frequency range of 0.1 Hz to 100 KHz with the applied AC signal amplitude of 10 mV.

3. RESULTS AND DISCUSSION

3.1. Structural analysis

The X-ray diffraction pattern of (a) pristine $LiMn_2O_4$ combustion product, (b) $LiNi_{0.05}Mn_{1.95}O_4$ combustion product, (c) pristine $LiMn_2O_4$ sample and (d) $LiNi_{0.05}Mn_{1.95}O_4$ sample are presented in Fig. 1.
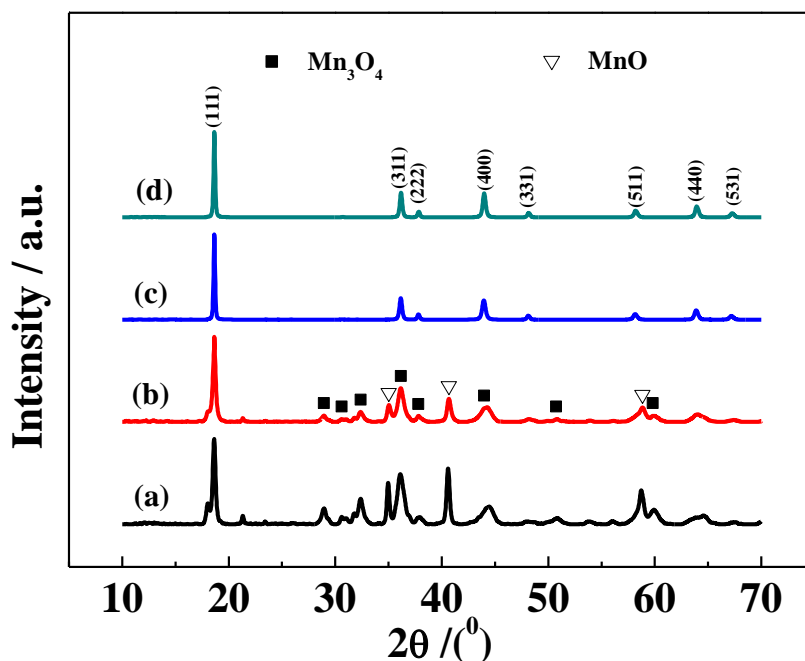
Figure 1. X-ray diffraction patterns of (a) pristine $LiMn_2O_4$ combustion product, (b) $LiNi_{0.05}Mn_{1.95}O_4$ combustion product, (c) pristine $LiMn_2O_4$ sample and (d) $LiNi_{0.05}Mn_{1.95}O_4$ sample.

We found that the peaks (2θ) at 18.71°, 36.22°, 37.86°, 44.06°, 48.25°, 58.29°, 63.94°and 67.21°were relative to the crystal planes of (111), (311), (222), (400), (331), (511), (440) and (531)

[35]. The diffraction patterns of the obtained combustion products and samples were indexed based on a cubic spinel $LiMn_2O_4$ (JCPDS card No. 35-0782) with the space group Fd3m [36]. There are typical Mn_3O_4 and MnO impurity peaks in the XRD patterns of the combustion products. When the $LiMn_2O_4$ combustion product was calcinated at 600 °C, the intensity of Mn_3O_4 impurity peaks obviously decrease and that of MnO impurity peaks completely disappear. When the $LiNi_{0.05}Mn_{1.95}O_4$ combustion product was calcinated at 600 °C for 3 hours, pure phase $LiNi_{0.05}Mn_{1.95}O_4$ can be obtained. It indicates that two-stage calcination and Ni-doping can successfully obtain the pure phase $LiNi_{0.05}Mn_{1.95}O_4$ [37, 38]. In addition, the $LiNi_{0.05}Mn_{1.95}O_4$ powder displayed sharper diffraction peaks than pristine $LiMn_2O_4$, because the $LiNi_{0.05}Mn_{1.95}O_4$ cathode material was more crystallized [39]. The lattice parameters calculated from XRD patterns were 8.2398 Å for $LiMn_2O_4$ and 8.2333 Å for $LiNi_{0.05}Mn_{1.95}O_4$. The lattice parameter of $LiNi_{0.05}Mn_{1.95}O_4$ was smaller than pristine $LiMn_2O_4$. This result was in accord with prior studies [25]. Since there is no ordering between Mn^{3+} and Mn^{4+} ions in the spinel lattice, that is, their distribution is random, Ni^{2+} ions do not substitute specifically Mn^{3+} ions, but doping increases the average manganese oxidation state. This consequently lowers the amount of Mn^{3+} ions, which are Jahn-Teller ions.

3.2. X-ray Photoelectron Spectroscopy
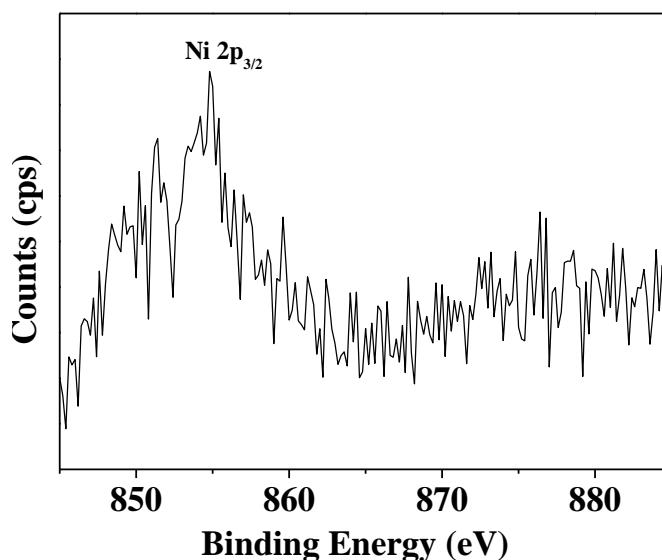
Figure 2. Ni 2p XPS spectra of the $LiNi_{0.05}Mn_{1.95}O_4$ powders.

The XPS binding energies are used to identify the oxidation states of different elements in materials. The Ni 2p XPS spectra of the $LiNi_{0.05}Mn_{1.95}O_4$ powders is shown in Fig. 2, It is shown in Fig. 2 that $LiNi_{0.05}Mn_{1.95}O_4$ gave the Ni $2p_{3/2}$ binding energy at 854.8 eV. It has been reported that Ni^{3+} and Ni^{2+} ion give rise to the Ni $2p_{3/2}$ binding energies at 855.8 eV and 854.5 eV, respectively [40]. As seen from Fig. 2, the Ni oxidation state of $LiNi_{0.05}Mn_{1.95}O_4$ was between +2 and +3, indicating partial Ni^{2+} cations were oxidized to Ni^{3+} in the material. Fig. 3 shows the Mn 2p XPS spectra of the pristine $LiMn_2O_4$ powders (a) and the $LiNi_{0.05}Mn_{1.95}O_4$ powders (b). The XPS spectra of Mn 2p can be

decomposed into two components (Mn $2p_{3/2}$ and Mn $2p_{1/2}$) due to the spin-orbital splitting [41]. It has been reported that Mn $2p_{3/2}$ binding energies of Mn^{3+} and Mn^{4+} are at 641.9 eV and 643.2 eV, respectively [42]. In this study, the Mn $2p_{3/2}$ binding energy of all two samples were in this region, which confirmed the average valence of Mn in $LiMn_2O_4$ and $LiNi_{0.05}Mn_{1.95}O_4$ are between +3 and +4 valence.
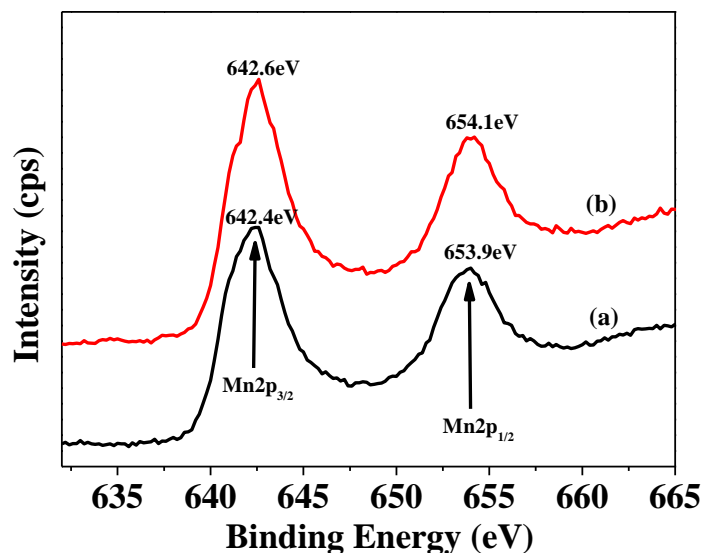
Figure 3. Mn 2p XPS spectra of the pristine $LiMn_2O_4$ powders (a) and the $LiNi_{0.05}Mn_{1.95}O_4$ powders (b).
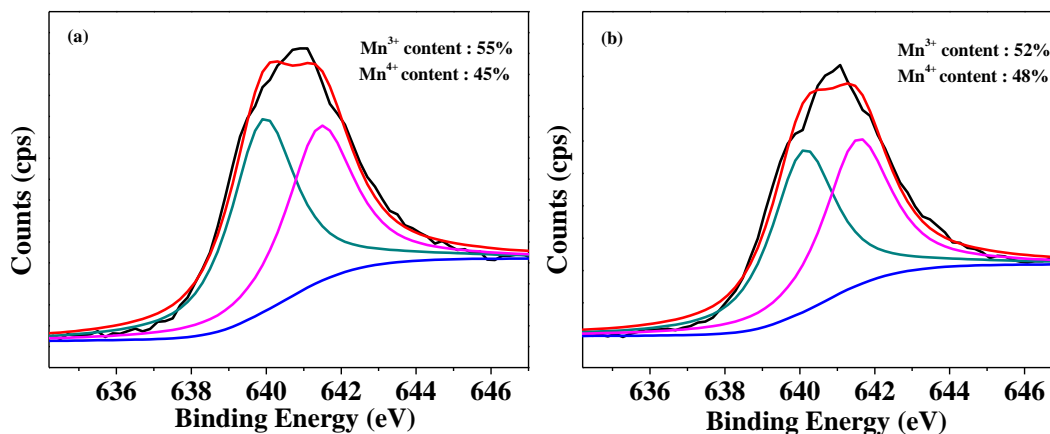
Figure 4. Deconvoluted profile of Mn $2p_{3/2}$ XPS spectra of the pristine $LiMn_2O_4$ powders (a) and the $LiNi_{0.05}Mn_{1.95}O_4$ powders (b).

The Mn $2p_{3/2}$ and Mn $2p_{1/2}$ peaks for $LiNi_{0.05}Mn_{1.95}O_4$ shifted to 642.6 and 654.1 eV, higher than 642.4 and 653.9 eV for $LiMn_2O_4$. The results suggest the Mn average valence of the spinel increases with doping of Ni, which is in favor of suppressing the Jahn-Teller distortion of the $LiMn_2O_4$ powders [43].

The relative amounts of Mn^{3+} and Mn^{4+} ions in $LiMn_2O_4$ and $LiNi_{0.05}Mn_{1.95}O_4$ can be estimated by deconvoluting the asymmetric Mn $2p_{3/2}$ XPS spectra were shown in Fig. 4. As shown in Fig. 4, the percentage of Mn^{3+} and Mn^{4+} ions of the undoped $LiMn_2O_4$ are 55% and 45%. For $LiNi_{0.05}Mn_{1.95}O_4$, the Mn^{3+} and Mn^{4+} amounts are about 52% and 48%, respectively. The $LiNi_{0.05}Mn_{1.95}O_4$ material exhibited a decreased Mn^{3+}/Mn^{4+} ratio and an increased average valance state in Mn, indicating the Ni substitution is likely to restrain the Jahn-Teller effect, which is helpful to the structural stability during charge-discharge cycling [44].

3.3. Morphology analysis
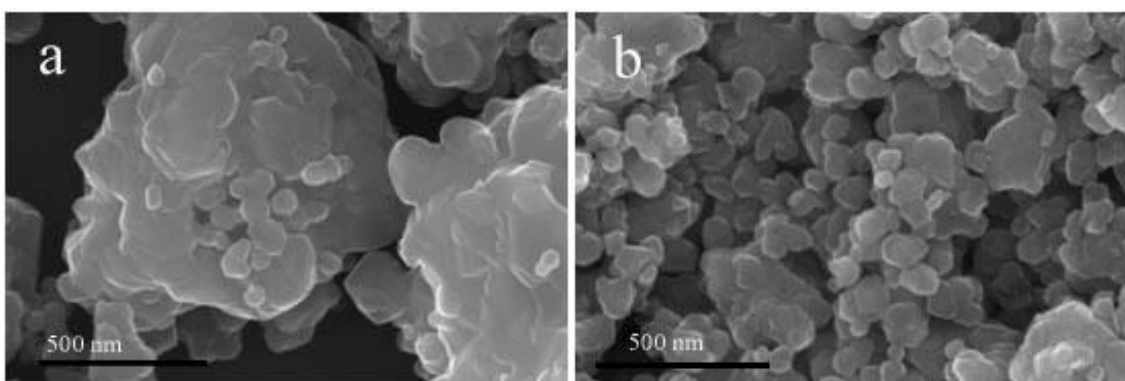
Figure 5. SEM images of (a) the pristine $LiMn_2O_4$ powders and (b) the $LiNi_{0.05}Mn_{1.95}O_4$ powders.

Fig. 5 (a) and (b) represent typical SEM images of the pristine and Ni doped $LiMn_2O_4$ samples, respectively. As shown in Fig. 5(a, b), the samples had agglomeration and irregular-shaped particles. No significant differences were found with the nickel substitute but for changes in particle size. The estimated particle size range for the pristine $LiMn_2O_4$ and $LiNi_{0.05}Mn_{1.95}O_4$ are 80~216 nm and 45~91 nm, respectively. TEM micrographs of the pristine and Ni doped $LiMn_2O_4$ samples are displayed in Fig. 6(a, b). Fig. 6(a, b) shows that the products had agglomeration.
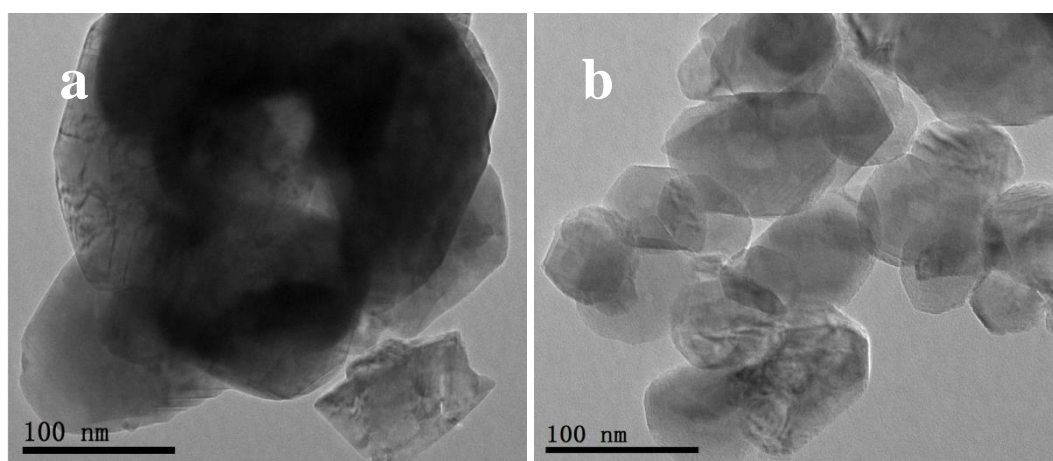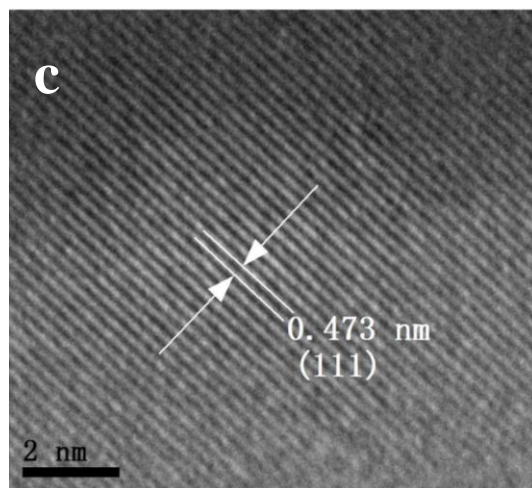
Figure 6. Transmittance electron micrographs of the pristine $LiMn_2O_4$ (a) and nano-$LiNi_{0.05}Mn_{1.95}O_4$ (b) powders; HRTEM image of nano-$LiNi_{0.05}Mn_{1.95}O_4$ (c).

The diameter of particles was approximately 180~200 nm for the $LiMn_2O_4$ and 50~90 nm for the $LiNi_{0.05}Mn_{1.95}O_4$. As a result, the pristine $LiMn_2O_4$ powders were submicroparticles , while the $LiNi_{0.05}Mn_{1.95}O_4$ powders were nanoparticles. In addition, the nano-$LiNi_{0.05}Mn_{1.95}O_4$ sample had a regular crystal form with noticeable edges and corners. The HR-TEM image of nano-$LiNi_{0.05}Mn_{1.95}O_4$ is presented in Fig. 6(c). Clear lattice fringes with a spacing of 0.473 nm were observed, which matched the d-value between the (111) diffraction planes of spinel $LiMn_2O_4$. It indicates that the nano-$LiNi_{0.05}Mn_{1.95}O_4$ sample had good crystallinity. This result was consistent with the XRD analysis discussed in Fig. 1.

3.4. Cyclic performance

Fig. 7(a) shows the initial charge/discharge profiles of the pristine $LiMn_2O_4$ and nano-$LiNi_{0.05}Mn_{1.95}O_4$ sample at current density of 148 mAh g^{-1} (1 C) between the potential rang 3.0-4.5 V (vs Li/Li$^+$) at room temperature. It can be obviously seen that all the samples display two voltage plateaus in the potential region of 3.9-4.2 V, which is typical for the two-phase lithium deintercalation/intercalation mechanism of the spinel $LiMn_2O_4$ electrode [39].
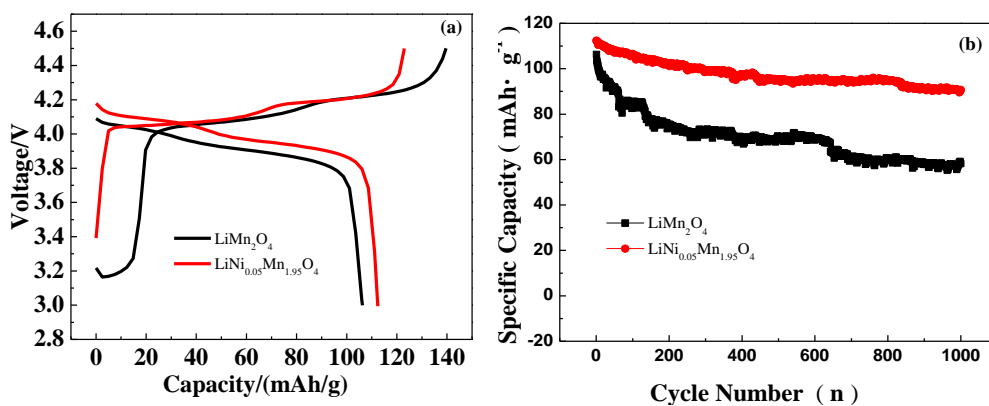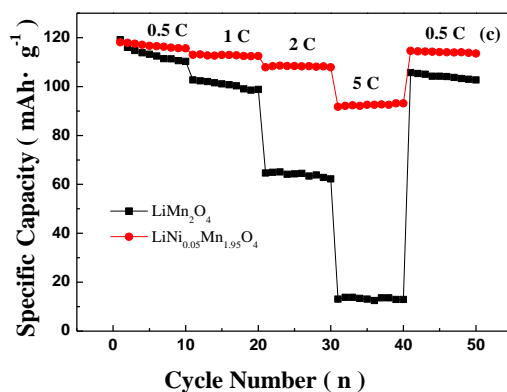
Figure 7. Charge-discharge profiles of the pristine $LiMn_2O_4$ and nano-$LiNi_{0.05}Mn_{1.95}O_4$ at 1 C (a). Cycling performance of the pristine $LiMn_2O_4$ and nano-$LiNi_{0.05}Mn_{1.95}O_4$ cell cycles between 3.0 and 4.5 V at the 1 C rate (b). Rate performances of the pristine $LiMn_2O_4$ and nano-$LiNi_{0.05}Mn_{1.95}O_4$ between 3.0 V and 4.5 V (c).

Table 1. The 1st and 1000th discharge capacities and capacity retention of the pristine $LiMn_2O_4$ and nano-$LiNi_{0.05}Mn_{1.95}O_4$ cathode materials.

Cathode materials	1st discharge capacity (mAh g^{-1})	1000th discharge capacity (mAh g^{-1})	Capacity retention (%)
$LiMn_2O_4$	106.3	58.2	54.8
$LiNi_{0.05}Mn_{1.95}O_4$	112.4	90.7	80.7

The profiles indicate that nano-$LiNi_{0.05}Mn_{1.95}O_4$ exhibits a higher discharge capacity than pristine $LiMn_2O_4$. Fig. 7(b) represents the cycling performance of undoped $LiMn_2O_4$ and nano-$LiNi_{0.05}Mn_{1.95}O_4$ samples at 1 C in the potential range between 3.0 and 4.5 V at room temperature.Table 1 summarizes the 1st and the 1000th discharge capacities and capacity retention. The $LiMn_2O_4$ electrode delivered an initial discharge capacity of approximately 106.3 mAh g^{-1} with a capacity retention of 54.8% after 1000 cycles, while the nano-$LiNi_{0.05}Mn_{1.95}O_4$ electrode released a higher initial capacity of 112.4 mAh g^{-1} with a capacity retention of 80.7% after 1000 cycles. The good cycling performance of nano-$LiNi_{0.05}Mn_{1.95}O_4$ are clearly attributable to nanoparticle and Ni doping. Prior researchers reported that the bond energy of Ni-O (1029 kJ mol^{-1}), which was stronger than that of Mn-O (946 kJ mol^{-1}), prevented Jahn-Teller distortion and stabilized the spinel structure of $LiMn_2O_4$ [23]. Fig. 7(c) shows the rate performances of $LiMn_2O_4$ and nano-$LiNi_{0.05}Mn_{1.95}O_4$ between 3.0 V and 4.5 V, which were measured at different rates ranging from 0.5 C to 5 C. The discharge capacity of the $LiMn_2O_4$ rapidly decreased when the charge-discharge rate increased. However, the nano-$LiNi_{0.05}Mn_{1.95}O_4$ electrode exhibited an improved high-rate capability, and its discharge capacity was 93.1 mAh g^{-1} even at 5 C. The improved rate capability could be attributed to the increased number of Mn^{4+} ions which enhance the ionic conductivity by lowering local Li diffusion activation

barriers [45]. Moreover, as the rate returned from 5 C to 0.5 C, the nano-$LiNi_{0.05}Mn_{1.95}O_4$ sample still delivered the discharge capacity of 114.6 mAh g^{-1} with better a recovery rate of 97%, compared to the recovery rate of 89% for the undoped $LiMn_2O_4$ sample. As such, the poor rate capability of the pristine $LiMn_2O_4$ was effectively improved by Ni doping, which were attributed to the Ni doping can suppresses the Jahn-Teller effect and the dissolution of Mn^{3+} [22].

3.5. Cyclic voltammetric studies
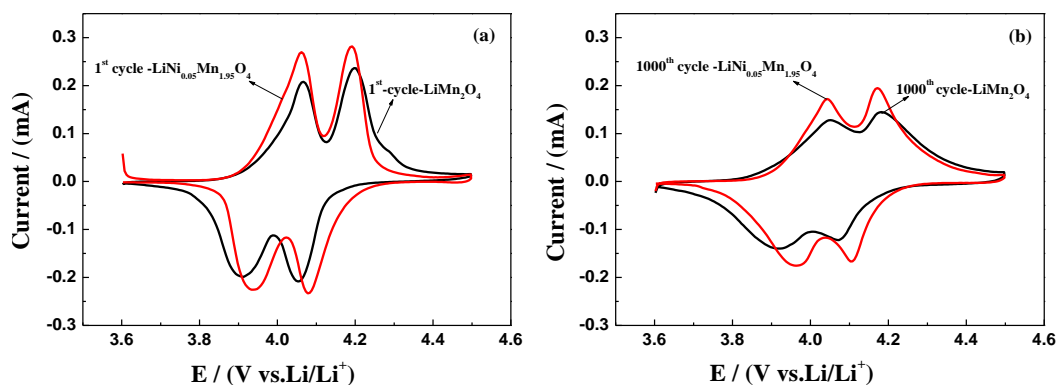
Figure 8. Typical CV curves of the initial cycle for the pristine $LiMn_2O_4$ and nano-$LiNi_{0.05}Mn_{1.95}O_4$ (a), typical CV curves of the 1000th cycles for both the pristine $LiMn_2O_4$ and nano-$LiNi_{0.05}Mn_{1.95}O_4$ (b).

Fig. 8 shows the typical cyclic voltammogram curves of the undoped $LiMn_2O_4$ and nano-$LiNi_{0.05}Mn_{1.95}O_4$ samples at a scan rate of 0.05 mV s^{-1} in the range of 3.6~4.5 V. The splitting of the redox peaks into two couples shows that the electrochemical reaction of the de-intercalation and intercalation of Li^+ ions consists of two processes [46, 47]. Fig. 8(a) shows the typical cyclic voltammogram curves of initial cycle for the undoped $LiMn_2O_4$ and nano-$LiNi_{0.05}Mn_{1.95}O_4$ samples. Fig. 8(b) presents the typical cyclic voltammogram curves of the 1000th cycle for both the undoped $LiMn_2O_4$ and nano-$LiNi_{0.05}Mn_{1.95}O_4$ samples. As depicted in Fig. 8(a) and (b), the nano-$LiNi_{0.05}Mn_{1.95}O_4$ sample had a higher peak compared to the peaks of the undoped $LiMn_2O_4$. These differences mean that the kinetic properties of the nano-$LiNi_{0.05}Mn_{1.95}O_4$ were better than the undoped $LiMn_2O_4$ material because Ni^{2+}-doping promoted the reversibility and the cycling retention of $LiMn_2O_4$.

The effects of the scan rates on the shape and peak current of CV are shown in Fig 9 (a) and (b), where the cyclic voltammograms of the pristine $LiMn_2O_4$ and nano-$LiNi_{0.05}Mn_{1.95}O_4$ at slow scan rates ranged from 0.02 to 0.2 mV s^{-1}. The peak current increased proportionally as the scan rates increased. With increasing scan rate, the separation between the two redox pairs becomes smaller. It is noted that the peaks of nano-$LiNi_{0.05}Mn_{1.95}O_4$ sample retain the well-defined shape when the scan rate increases to 0.2 mV s^{-1} (Fig. 9 (b)), which indicates that the nano-$LiNi_{0.05}Mn_{1.95}O_4$ electrodes can be charged and discharged at larger current densities. In contrast, the peaks of the undoped $LiMn_2O_4$ become less distinguishable at this scan rate (Fig. 9(a)) [48].
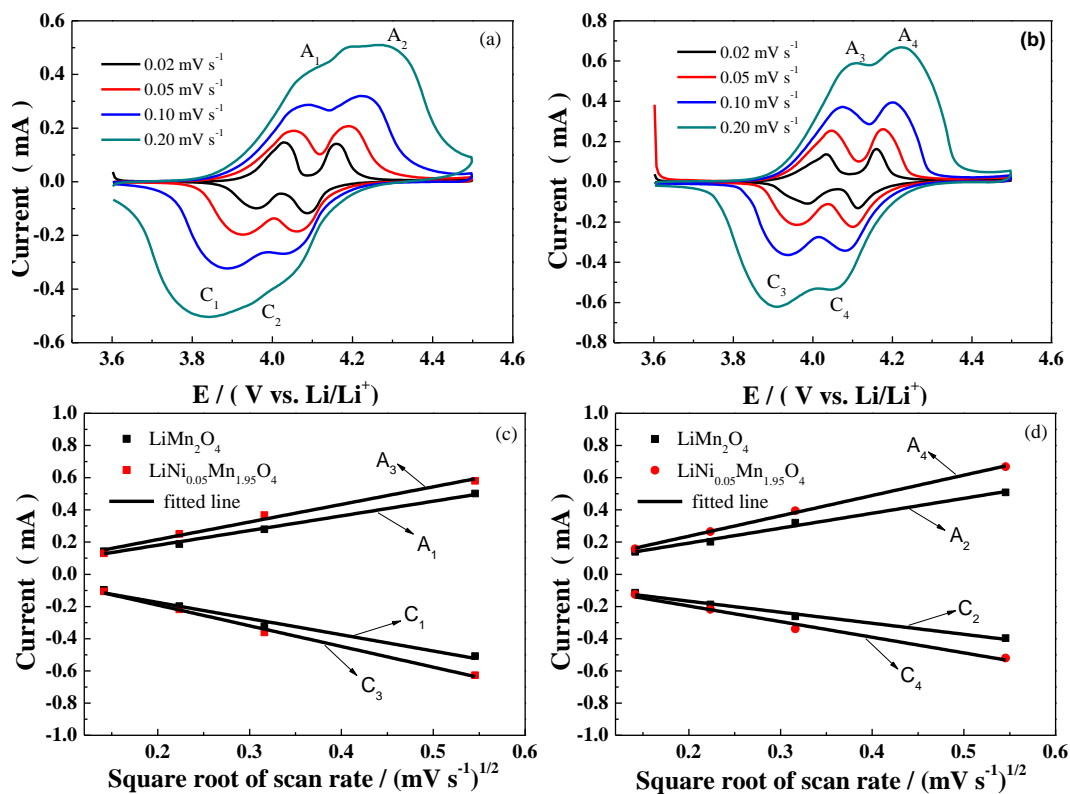
Figure 9. The cyclic voltammograms of the pristine $LiMn_2O_4$ (a) and nano-$LiNi_{0.05}Mn_{1.95}O_4$ (b) at different scan rates. Plots of peak current vs. square root of the scan rate for the pristine $LiMn_2O_4$ (c) and nano-$LiNi_{0.05}Mn_{1.95}O_4$ (d).

The plots of the peak currents versus the square root of the scan rates of two samples had a good linear relationship, as shown in Fig 9 (c) and (d). These results indicated that Li^+ intercalation and de-intercalation was a diffusion-controlled process [35]. For a reversible reaction involving Li-ion diffusion behavior, the chemical diffusion coefficient of Li-ion can be obtained by the Randles-Sevcik equation [49]:

$$I_p = 2.69 \times 10^5 n^{3/2} A D^{1/2} C v^{1/2} \qquad (1)$$

where I_p is the peak current value (A), n is the number of electrons per reaction species (for Li^+ n = 1), A is the area of the electrode (2.01 cm^2 in this case), C is the bulk concentration of the lithium ion in the electrode (0.0238 mol cm^{-3} for $LiMn_2O_4$ derived from the theoretical density of 4.3 g cm^{-3}), D is the chemical diffusion coefficient ($cm^2 s^{-1}$), and V is the scan rate ($V s^{-1}$). According to Eq. (1), the diffusion coefficients (D) of the pristine $LiMn_2O_4$ and nano-$LiNi_{0.05}Mn_{1.95}O_4$ are calculated to be 5.94×10^{-13} and 7.64×10^{-13} $cm^2 s^{-1}$, respectively, as indicated in Fig. 9 (c) and (d). The faster lithium-ion diffusion is attained for the increased value of D with nano-$LiNi_{0.05}Mn_{1.95}O_4$, which definitely improves the rate capability. The increase of D can be attributed to the enlargement of the inter-slab distance for the layer-layer material, which provides more space for lithium-ion to diffuse among the electrode materials [50].

3.6. Electrochemical impedance spectroscopy (EIS)
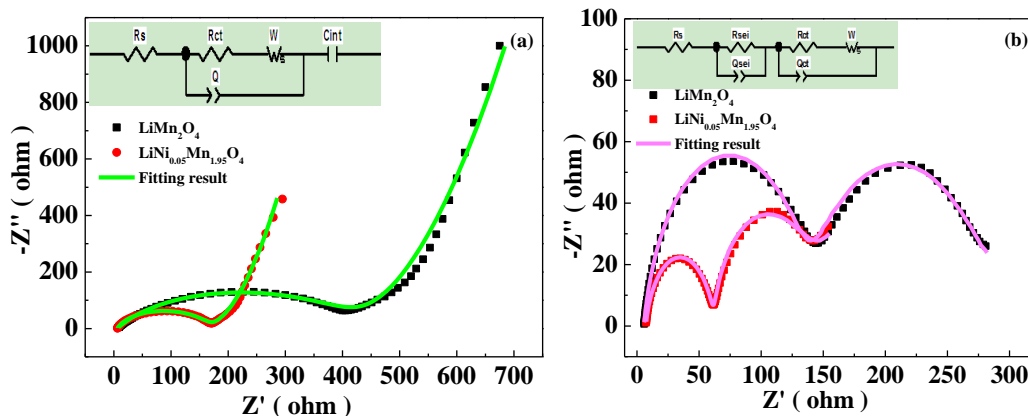
Figure 10. The EIS plots of the pristine $LiMn_2O_4$ and nano-$LiNi_{0.05}Mn_{1.95}O_4$ samples after 50th (a) and 1000th (b) cycles. Inset: the equivalent circuit for EIS results fitting.

Fig. 10 shows the Nyquist plots of the pristine $LiMn_2O_4$ and nano-$LiNi_{0.05}Mn_{1.95}O_4$ samples after 50th (a) and 1000th (b) cycles.

Table 2. Impedance parameters obtained using equivalent circuit models for the pristine $LiMn_2O_4$ and nano-$LiNi_{0.05}Mn_{1.95}O_4$ samples after 50th cycles

Parameter	Cathode material	
	$LiMn_2O_4$	$LiNi_{0.05}Mn_{1.95}O_4$
R_s (Ω)	6.1	6.3
R_{ct} (Ω)	414.5	159.0
Q	1.8×10^{-5}	9.6×10^{-6}
W (Ω)	3.3×10^{-3}	7.4×10^{-3}
C_{int} (mF)	2.2×10^{-3}	4.7×10^{-5}

Table 3. Impedance parameters obtained using equivalent circuit models for the pristine $LiMn_2O_4$ and nano-$LiNi_{0.05}Mn_{1.95}O_4$ samples after 1000th cycles

Parameter	Cathode material	
	$LiMn_2O_4$	$LiNi_{0.05}Mn_{1.95}O_4$
R_s (Ω)	5.6	7.2
R_{sei} (Ω)	130.6	54.5
Q_{sei}	9.1×10^{-6}	7.6×10^{-6}
R_{ct}(Ω)	145.7	75.7
Q_{ct}	1.1×10^{-3}	1.4×10^{-3}
W (Ω)	9.4×10^{-4}	3.9×10^{-2}

The equivalent circuit is also shown in the inset of Fig. 10(a, b). The values of the parameters obtained from fitting the experimental impedance spectra are listed in Table 2 and 3. R_s was the solution resistance corresponding to the high frequency intercept at the Z' axis. The first semicircle at high frequency represents the impedance (R_{sei}) is related to the formation of the passivation film on the surface of the cathode material [51]. The capacitances of the double layer are represented by the constant phase elements Q_{sei} and Q_{ct} (Q), respectively. The second semicircle at medium frequency reveals the Li^+ charge transfer resistance (R_{ct}) at the electrode-electrolyte interfaces.

The low frequency tail corresponded to Warburg impedance (W), which was associated to Li^+ diffusion in the $LiMn_2O_4$ particles [52-54]. In Fig. 10(a), only one semicircle is observed in the electrode after 50th charge-discharge cycles. It is suggested that the surface film is not formed yet, because of the absence of passive film resistance and its relative capacitance [55]. As shown in Table 2, the charge-transfer resistance of nano-$LiNi_{0.05}Mn_{1.95}O_4$ was only 159 Ω, which was less than that of the pristine $LiMn_2O_4$ (414.5 Ω). Therefore, Ni ion doping improved the charge transfer ability in charging and discharging process and then increased the rate capability and the cycle performance. As shown in Fig. 10 (b), the two semicircles are observed in the electrode after 1000th charge-discharge cycles, which indicated that a stable SEI layer has been formed [56]. As shown in Table 3，It is apparently to see the values of R_{sei} for the nano-$LiNi_{0.05}Mn_{1.95}O_4$ (54.54 Ω) are lower than that of the pristine $LiMn_2O_4$ (130.6 Ω), and the R_{ct} of the nano-$LiNi_{0.05}Mn_{1.95}O_4$ (75.66 Ω) is also lower than that of the pristine $LiMn_2O_4$. This indicates that the Ni-doping can indeed restrain side-reactions which may cause the formation of unwanted resistive layers and continued growth of cell impedance [25].

3.7. XRD test of before and after cycling

Fig. 11(a) and (b) shows the XRD patterns of the pristine $LiMn_2O_4$ and nano-$LiNi_{0.05}Mn_{1.95}O_4$ electrodes after initial and 1000th cycles, respectively, in which the XRD peaks of Al are denoted by (☆). A small amount of an impurity phase is detected in the XRD patterns ($2\theta=28.6°$), because the working electrode includes 80 wt.% active materials, 10 wt.% super P carbon black and 10 wt.% polyvinylidene fluoride (PVDF).
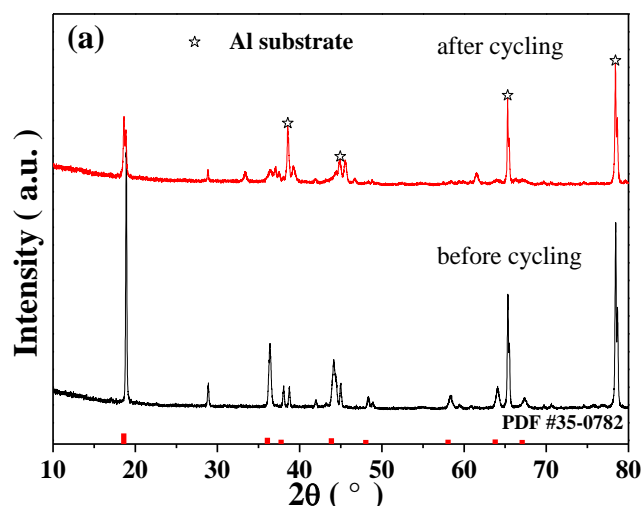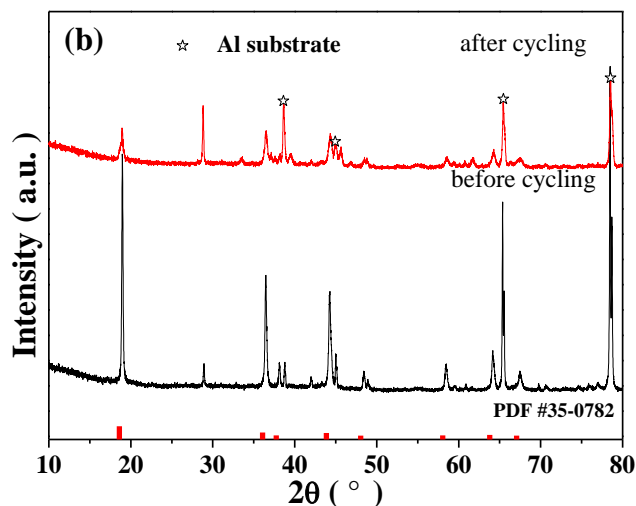
Figure 11. XRD patterns of electrodes before and after cycling: the pristine $LiMn_2O_4$ spinel cathode (a) and the nano-$LiNi_{0.05}Mn_{1.95}O_4$ spinel cathode (b).

Undoped $LiMn_2O_4$ electrode has obviously reduced the finger print XRD peaks after 1000th cycle. This depicts to increase the lattice disorder and decrease the crystallinity. In contrast, the nano-$LiNi_{0.05}Mn_{1.95}O_4$ electrode has slightly changes in the peak intensities of the finger print XRD peaks after the 1000th cycle. Implying that Ni-ion doping can improve the structural stability of $LiMn_2O_4$ during cycling, retard the side reactions between the electrode and electrolyte and further minimize the Mn dissolution during cycling process and result in a better cycleability and rate capability.

4. CONCLUSIONS

A single-phase spinel structure was synthesized for the nano-$LiNi_{0.05}Mn_{1.95}O_4$ sample using a low temperature molten-salt combustion method. The nano-$LiNi_{0.05}Mn_{1.95}O_4$ cathode material was developed and consisted of agglomeration particles with sizes of 50~90 nm. Compared with pristine $LiMn_2O_4$, the nano-$LiNi_{0.05}Mn_{1.95}O_4$ cathode material exhibited improved capacity retention. The capacity retention of nano-$LiNi_{0.05}Mn_{1.95}O_4$ was 80.7% after 1000 cycles at 1 C at room temperature. At 5 C, the discharge capacity was 93.1 mAh g^{-1}. The electrochemical studies demonstrated that the nano-$LiNi_{0.05}Mn_{1.95}O_4$ cathode material had a high cyclic performance and good reversibility. The electrochemical behaviors in the CV and EIS tests suggested that the Ni-doped sample had better electrochemical reversibility and kinetics. In addition, the XRD test before and after cycling revealed that the nano-$LiNi_{0.05}Mn_{1.95}O_4$ material after 1000 cycles at 1 C was well crystallized with a stable structure.

References

1. D. Arumugam, G. P. Kalaignan, *J. Electroanal. Chem.* 648 (2010) 54-59.
2. L.F. Xiao, Y.Q. Zhao, Y.Y. Yang, Y.L. Cao, X.P. Ai, H.X. Yang, *Electrochim. Acta* 54 (2008) 545-550.
3. B. Ebin, S. Gürmen, G. Lindbergh, *Ceram. Int* 40 (2014) 1019-1027.
4. H.Q. Wang, F.Y. Lai, Y. Li, X.H. Zhang, Y.G. Huang, S.J. Hu, Q.Y. Li, *Electrochim. Acta* 177 (2015) 290-297.
5. O.S. Mendoza-Hernandez, H. Ishikawa, Y. Nishikawa, Y. Maruyama, Y. Sone, M. Umeda, *J. Solid State Electrochem.* 19 (2015) 1203-1210.
6. S.N. Kwon, H. R. Park, M.Y. Song, *Ceram. Int* 40 (2014) 11131-11137.
7. D. Arumugam, G.P. Kalaignan, P. Manisankar, *J. Solid State Electrochem.* 13 (2009) 301-307.
8. M.S. Wang, J. Wang, J. Zhang, L.Z. Fan, *Ionics* 21 (2015) 27-35.
9. C.G. Han, C.Y. Zhu, G. Saito, T. Akiyama, *RSC Adv.* 5 (2015) 73315-73322.
10. X. Yi, X.Y. Wang, B.W. Ju, Q.L. Wei, X.K. Yang, G.S. Zou, H.B. Shu, L. Hu, *J. Alloys Compd.* 604 (2014) 50-56.
11. A. Lturrondobeitia, A. Goni, L. Lezama, C. Kim, M. Doeff, J. Cabana, T. Rojo, *J. Mater. Chem. A*, 1 (2013) 10857-10862.
12. C.G. Han, Chunyu Zhu, G. Saito, T. Akiyama, *Electrochim. Acta* 209 (2016) 225-234.
13. R. Thirunakaran, G.H. Lew, W.S. Yoon, *J. Electroanal. Chem.* 767 (2016) 141-152.
14. H.Y. Zhao, S.S. Liu, Z.W. Wang, Y. Cai, M. Tan, *Electrochim. Acta* 199 (2016) 18-26.
15. Y.S. Shi, S.M. Zhu, C.L. Zhu, Y. Li, Z.X. Chen, D. Zhang, *Electrochim. Acta* 154 (2015) 17-23.
16. J.B. Hao, H.L. Bai, J.T. Liu, F.L. Yang, Q.L. Li, C.W. Su, J.M. Guo, *J. Alloys Compd.* 668 (2016) 200-205.
17. A. Iturrondobeitia, A. Goni, V. Palomares, I.G. Muro, L. Lezama, T. Rojo, *J. Power Sources* 216 (2012) 482-488.
18. D.L. Guo, B. Li, Z.R. Chang, H.W. Tang, X.H. Xu, K. Chang, E.B. Shangguan, X.Z. Yuan, H.J. Wang, *Electrochim. Acta* 134 (2014) 338-346.
19. H.M. Wu, J.P. Tu, X.T. Chen, Y. Li, X.B. Zhao, G.S. Cao, *J. Solid State Electrochem.* 11 (2007) 173-176.
20. L.L. Xiong, Y.L. Xu, T. Tao, J.B. Goodenough, *J. Power Sources* 199 (2012) 214-219.
21. H.Y. Zhao, S.S. Liu, Z.W. Wang, Y. Cai, M. Tan, X.Q. Liu, *Ceram. Int* 42 (2016) 13442-13448.
22. Q.Q. Wang, X.S. Zhang, Y.L. Xu, D. Liu, H. Dong, Y. Zhang, *RSC Adv.* 5 (2015) 75333-75340.
23. F.X. Wang, S.Y. Xiao, Y. Shi, L.L. Liu, Y.S. Zhu, Y.P. Wu, J.Z. Wang, R. Holze, *Electrochim. Acta* 93 (2013) 301-306.
24. Q.L. Wei, X.Y. Wang, X.K. Yang, B.W. Ju, B.N. Hu, H.B. Shu, W.C. Wen, M. Zhou, Y.F. Song, H. Wu, H. Hu, *J. Mater. Chem. A.* 1 (2013) 4010-4016.
25. M.A. Kebede, N. Kunjuzwa, C.J. Jafta, M.K. Mathe, K.I. Ozoemena, *Electrochim. Acta* 128 (2014) 172-177.
26. J.M. Amarilla, R.M. Rojas, F. Pico, L. Pascual, K. Petrov, D. Kovacheva, M.G. Lazarraga, I. Lejona, J.M. Rojo, *J. Power Sources* 174 (2007) 1212-1217.
27. Y.J. Cai, Y.D. Huang, X.C. Wang, D.Z. Jia, X.C. Tang, *Ceram. Int* 40 (2014) 14039-14043.
28. V. G. Kumar, J. S. Gnanaraj, S. B. David, D. M. Pickup, E. R. H. van-Eck, A. Gedanken, D. Aurbach, *Chem. Mater.* 15 (2003) 4211-4216.
29. X.N. Ding, H.W. Zhou, G.C. Liu, Z. Yin, Y. Jiang, X.D. Wang, *J. Alloys Compd.* 632 (2015) 147-151.
30. X.F. Gao, Y.J. Sha, Q. Lin, R. Cai, M.O. Tade, Z.P. Shao, *J. Power Sources* 275 (2015) 38-44.
31. H.K. Kang, W. Ahn, S.G. Lee, K.S. Han, J.H. Song, O.H. Kwon, E.Y. Kang, *J. Power Sources* 163 (2006) 166-172.

32. J.J. Huang, F.L. Yang, Y.J. Guo, C.C. Peng, H.L. Bai, J.H. Peng, J.M. Guo, *Ceram. Int* 41 (2015) 9662-9667.
33. H. Weitz, A.M. Garbers-Craig, *MINERAL PROCESSING AND EXTRACTIVE METALLURGY REVIEW* 37 (2016) 268-178.
34. H.Weitz, A. Garbers-Craig, *Advances in Molten Slags, Fluxes, and Salts: Proceedings of The 10th International Conference on Molten Slags, Fluxes and Salts* (MOLTEN16) (2016) 87-95.
35. M.W. Xiang, C.W. Su, L.L. Feng, M.L. Yuan, J.M. Guo, *Electrochim. Acta* 125 (2014) 524-529.
36. S. Mandal, R. M. Rojas, J. M. Amarilla, P. Calle, N. V. Kosova,V. F. Anufrienko, J.M. Rojo, *Chemistry of Materials*14 (2002) 1598-1605.
37. B.J. Hwang, R. Santhanam, S.G. Hu, *J. Power Sources* 108 (2002) 250-255.
38. T. Qiu, J. Wang, Y.L. Lu, W.S. Yang, *Electrochim. Acta* 147 (2014) 626-635.
39. D.L. Fang, J.C. Li, X. Liu, P.F. Huang, T.R. Xu, M.C. Qian, C.H. Zheng, *J. Alloys Compd.* 640 (2015) 82-89.
40. K.S. Kim, N. Winograd, *Surf. Sci.* 43 (1974) 625-643.
41. X.F. Chu, K.K. Huang, M. Han, S. Feng, *Inorg. Chem.* 52 (2013) 4130-4132.
42. K.M. Shaju, G.V. Subba Rao, B.V.R. Chowdari, *Solid State Ionics* 69 (2002) 152-153.
43. Y.J. Wei, L.Y. Yan, C.Z. Wang, X.G. Xu, F. Wu, G. Chen, *J. Phys. Chem. B* 108 (2004) 18547-18551.
44. K.J. Kim, J.H. Lee, *Solid State Commun.* 141 (2007) 99-103.
45. Y. Xu, G. Chen, E.G. Fu, M. Zhou, M. Dunwell, L. Fei, S.G. Deng, P. Andersen, Y.Q. Wang, Q.X. Jia, H.M. Luo, *RSC Adv.* 3 (2013) 18441-18445.
46. F.P. Nkosi, C.J. Jafta, M. Kebede, L. Roux, M. K. Mathe, K.I. Ozoemena, *RSC Adv.* 5 (2015) 32256-32262.
47. A.B. Yuan, L. Tian, W.M. Xu, Y.Q. Wang, *J. Power Sources* 195 (2010) 5032-5038.
48. C.W. Liang, D. Fang, Y.H. Cao, G.Z. Li, Z.P. Luo, Q.H. Zhou, C.X. Xiong, W.L. Xu, *J. Colloid Interface Sci.* 439 (2015) 69-75.
49. B.M. Hwang, S.J. Kim, Y.W. Lee, H.C. Park, D.M. Kim, K.W. Park, *Mater. Chem. Phys.* 158 (2015) 138-143.
50. X. Jin, Q.J. Xu , H.M. Liu, X.L. Yuan, Y.Y. Xia, *Electrochim. Acta* 136 (2014) 19-26.
51. Y.J. Cai, Y.D. Huang, X.C. Wang, D.Z. Jia, W.K. Pang, Z.P. Guo, Y.P. Du, X.C. Tang, *J. Power Sources* 278 (2015) 574-581.
52. H.Q. Wang, F.Y. Lai, Y. Li, X.H. Zhang, Y.G. Huang, S.J. Hu, Q.Y. Li, *Electrochim. Acta* 177 (2015) 290-297.
53. T. Shi, Y. Dong, C.M. Wang, F. Tao, L. Chen, *J. Power Sources* 273 (2015) 959-965.
54. C.H. Zheng, Z.F. Wu, J.C. Li, X. Liu, D.L. Fang, *Ceram. Int* 40 (2014) 8455-8463.
55. R.H. Wang, X.H. Li, Z.X. Wang, H.J. Guo, M.R. Su, T. Hou, *J. Alloys Compd.* 624 (2015) 74-84.
56. G.S. Zou, X.K. Yang, X.Y. Wang, L. Ge, H.B. Shu, Y.S. Bai, C. Wu, H.P. Guo, L. Hu, X. Yi, B.W. Ju, H. Hu, D. Wang, R.Z.Yu, *J. Solid State Electrochem.* 18 (2014) 1789-1797.